





## Article

# On the Representativeness of Proton Radiation Resistance Tests on Optical Coatings for Interplanetary Missions

Anna Sytchkova <sup>1,\*</sup>, Maria Lucia Protopapa <sup>2</sup>, Paolo Olivero <sup>3</sup>, Zicai Shen <sup>4</sup> and Yanzhi Wang <sup>5</sup><sup>1</sup> ENEA Optical Coatings Group, TERIN-DEC-CCT, C.R. Casaccia, via Anguillarese 301, 00123 Rome, Italy<sup>2</sup> ENEA SSPT-PROMAS-MATAS, C.R. Brindisi, SS 7 Appia Km 706, 72100 Brindisi, Italy; lucia.protopapa@enea.it<sup>3</sup> Physics Department, University of Torino, via P. Giuria 1, 10125 Torino, Italy; paolo.olivero@unito.it<sup>4</sup> Beijing Institute of Spacecraft Environment Engineering, Beijing 100094, China; zicaishen@163.com<sup>5</sup> Laboratory of Thin Film Optics, Shanghai Institute of Optics and Fine Mechanics, No. 390 Qinghe Road, Jiading District, Shanghai 201800, China; yanzhiwang@siom.ac.cn

\* Correspondence: anna.sytchkova@enea.it

**Abstract:** Optical instrumentation used in space normally employs optical coatings. Future interplanetary space missions will be characterized by ever longer stays in environmental conditions where low energy protons represent one of the main types of radiation impacting the coating longevity and performance. To ensure the reliability of coated optics, environmental resistance tests should be accurately planned to be representative for a mission. To this end, the existing standards for coating tests and the test results interpretation have been constantly improved. In this study, we analyze the relevant standards of the European Space Agency (ESA) and of the Chinese Space Agency (CSA) for testing coated optics for interplanetary missions, and in particular for the missions at the Lagrange points. We focus in particular on the applicability of these standards and hence on their possible refinement when specifically implemented to the optical thin films and coatings. We proceed with the development of a methodology for reliable interpretation of the proton irradiation tests for the optical coatings for interplanetary missions, first briefly overviewing the existing tools which allow for space environment simulation and hence deriving the test conditions for the Lagrange points. Furthermore, we apply the approach to testing of aluminum oxide optical coatings for applications in the visible spectral range, concluding on the representativeness of the proposed approach and on possible refinement of the existing standards for coating tests when they are specifically developed for optical applications.

**Keywords:** optical coatings; space environment; ground simulation test; space test standards; proton irradiation; proton-induced damage; optical instruments; interplanetary missions; Lagrange points; aluminum oxide



**Citation:** Sytchkova, A.; Protopapa, M.L.; Olivero, P.; Shen, Z.; Wang, Y. On the Representativeness of Proton Radiation Resistance Tests on Optical Coatings for Interplanetary Missions. *Coatings* **2024**, *14*, 898. <https://doi.org/10.3390/coatings14070898>

Academic Editor: Panos Pouloupoulos

Received: 7 June 2024

Revised: 3 July 2024

Accepted: 16 July 2024

Published: 18 July 2024



**Copyright:** © 2024 by the authors. Licensee MDPI, Basel, Switzerland. This article is an open access article distributed under the terms and conditions of the Creative Commons Attribution (CC BY) license (<https://creativecommons.org/licenses/by/4.0/>).

## 1. Introduction

Space exploration is of fundamental economic and social importance. CubeSat [1,2] and SmallSat missions [3] paved the way to lower the costs of scientific space programs and to the commercial exploitation of space, with a perspective of ever-deeper space missions. Nowadays, the two world major alliances for the peaceful exploration of space, which are the Artemis Accords [4] led by the USA and the ILRS [5] led by China, are working on a series of lunar and deep space missions. The countries invest in exploration of the solar system aiming for the colonization of nearby space and exploitation of the resources other planets and asteroids may make available.

Every space mission requires a dedicated study for modeling the conditions for the environment a spacecraft will work in or fly through. Challenging conditions for coated surfaces in interplanetary environment are represented mainly by corpuscular radiation, by intense electromagnetic radiation (cosmic and gamma rays), and by cryogenic temperatures.

For a given scenario of equipment exploitation, the laboratory testing on the materials behaviour is meaningful when radiation fluence conditions are reproduced. Consequently, the estimation of the energetic particle background in the regions of the spacecraft mission is the starting task for the device designers, as adequate knowledge of the radiation environment allows ensuring of equipment functionality.

Among the corpuscular components, there are charged particles like protons, electrons and a wide variety of ions, with different degrees of ionisation and energies ranging from fractions of keVs up to EeVs [6]. Most protons originate from the Sun, and solar wind simulations are needed (e.g., [7]) to take into account the radiation level for the period chosen for a mission. Soon after launch, a spacecraft is exposed to the low-energy proton belts (30 keV) formed near Earth [8]. Such charged particles pass through materials, slowing down as they lose energy along the way. When their energy is insufficient to pass through, the incoming particles come into rest and deposit all the remaining energy. Higher energy particles travel through the spacecraft shielding and reach even the innermost region, where they can harm optical and opto-electronic devices [9].

Coatings are widely used in spacecrafts both for shielding and for the on-board instrumentation. Thin films and optical coatings are mostly affected by low energy particles which deposit their energies along the coating thickness and rest inside the coating. The energy range of charged particles is very vast, so low energy particles are present both outside and inside the spacecraft. Although the fluences of low energy particles may be different for different positions of a coating outside or inside the spacecraft, these low energy particles are present everywhere during the mission and the coating may suffer from their impact.

As an example of an ESA large-class mission with optical devices which may be affected by so-called soft protons or low-energy protons (those with energies in the range from tens to hundreds of keV) is the Advanced Telescope for High Energy Astrophysics (ATHENA), planned for launch in 2030. It consists of a large X-ray telescope and two focal plane instruments with complementary capabilities: the Wide Field Imager and the X-ray Integral Field Unit (X-IFU). Low-energy protons are those which mostly impact the X-ray mirrors and, funneling toward the focal plane, they also impact the detectors. Both phenomena may induce operational problems at increased soft proton background fluxes, like what happened in earlier missions.

Since the earliest comprehensive systematic monographs on space environment modeling (e.g., [10]), numerous groups of scientists and engineers have been involved in the development of models and improvement of existing tools. Nowadays, leading space agencies and research institutions in the field may profit from a variety of theoretical and numerical methods. For example, the NASA website provides a list of software, models, and tools available on space environment simulation [11], including links for downloads and references. The task is complex, and even artificial intelligence for modeling of the space environment has been attempted [12]. Recently, an overview of available models for proton radiation simulations in interplanetary space was published, and the proton energy spectra obtained by different models were compared [13]. However, the aforementioned systematic studies report data for particles with energies higher than 100 keV, while thin films and optical coatings with their nanometric-range thicknesses are mostly affected by particles with much lower energies.

Therefore, this study begins with estimation of the radiation background in the Lagrange points, which are among the most representative positions in interplanetary space for astrophysics and astronomy missions. We analyse how the existing models can extrapolate the low energy particle background using recent experimental data. We also analyse the relevant European and Chinese standards and propose steps for better representativeness in these tests. The existing standards for space environmental tests on coatings have been developed for generic uses like shielding resistance to particle radiation [14,15], and the specifics of the optical coatings has been insufficient. In Section 4, we formulate a rigorous approach for radiation testing of optical coatings based on the application of the existing

standards, which were critically analysed in Section 3 for the space environment modelled in Section 2. Finally, Section 5 provides an example of a single-layer material study applying the developed methodology.

## 2. Space Environment Modeling in L1 and L2 Points

In 1772, Joseph Louis de Lagrange demonstrated that a gravitationally bound binary system, such as the Sun-Earth system, has five specific stationary points where the gravitational forces and the centripetal force are in perfect balance. These points are known as Lagrange Points. At these locations, a small object can theoretically remain in a stable position relative to the two larger bodies [16]. Of the five Lagrange points, three are unstable (L1, L2, and L3) and lie along the line connecting the two massive objects. The remaining two points, L4 and L5, are stable and form the vertices of equilateral triangles with the two large bodies at the other vertices.

Many satellites have been positioned at the Lagrange points, particularly L1 and L2. Satellites located at the L1 point of the Earth-Sun system have an uninterrupted view of the Sun, making it an ideal location for monitoring solar wind. The solar wind reaches this point about one hour before reaching Earth, allowing for advanced in situ measurements. Satellites at L1 provide valuable data on solar wind plasma, including speed, temperature, direction, electron and ion distributions, protons and alpha-particles, as well as the electromagnetic field, to study energetic particles accelerated in situ and/or near the Sun [17]. In 1995, the Solar and Heliospheric Observatory Satellite (SOHO) was placed at L1, approximately 1.5 million kilometers from Earth. Several other space missions, such as WIND, the Solar and Heliospheric Observatory, the Advanced Composition Explorer (ACE), and Earth observatories like the Deep Space Climate Observatory, are also located near Lagrange point L1 [12].

The L2 point of the Earth-Sun system has hosted several spacecraft, including the Wilkinson Microwave Anisotropy Probe (WMAP), Planck, Herschel, and the James Webb Space Telescope (JWST). The L2 point is particularly advantageous for astronomy because a spacecraft positioned there can maintain reliable communication with Earth, keep the Sun behind Earth and the Moon to generate energy via solar panels, and—with appropriate shielding—provide telescopes with clear view of deep space. However, it is important to note that the L1 and L2 points are unstable on a timescale of approximately 23 days, necessitating regular orbital corrections for satellites stationed in these positions.

Interplanetary environments are characterized by several ionizing radiation components with different origins, such as galactic cosmic rays (GCRs) and solar energetic particles (SEPs). GCRs and SEPs are influenced by the interplanetary magnetic field, evolving over timescales ranging from a few hours to several years, primarily driven by short- and long-term processes related to solar activity. These processes include solar rotational periodicities, quasi-biennial oscillations, and the Schwabe cycle. The more in-detail Schwabe cycle is an approximately 11-year periodic change in the Sun's activity, measured by variations in the number of observed sunspots on the Sun's surface. Throughout a solar cycle (SC), levels of solar radiation and material ejection, the number and size of sunspots, solar flares, and coronal loops all fluctuate in a synchronized pattern from a period of minimum activity to maximum activity and back to minimum activity. Solar cycle 24, the most recently completed SC, is the 24th cycle since 1755, when extensive recording of solar sunspot activity began.

While GCRs provide a continuous high-energy proton flux, SEP events are short-lived hazards that can vary in both total flux and energy spectral characteristics from one event to another. Investigating radiation components and the high-energy particle background is of primary importance for any space mission profile. To this end, particularly for interplanetary environments, the European Space Agency (ESA) developed a web-based space environment tool called SPENVIS [18]. This tool allows users to generate a spacecraft trajectory or a coordinate grid and then calculate the following:

- Geomagnetic coordinates
- Electron fluxes and solar proton fluences
- Radiation doses (ionizing and non-ionizing) for simple geometries
- Sectoring analysis for dose calculations in more complex geometries
- Damage equivalent fluences for Si, GaAs, and multi-junction solar cells
- Geant4 Monte Carlo analysis for doses and pulse height rates in planar and spherical shields
- Ion Linear Energy Transfer (LET) and flux spectra and single event upset rates

In this study, we are particularly interested in the simulation of solar proton fluxes. Due to the lack of models for solar wind, it is necessary to use data from solar observatories, which are sparse. Solar wind flow data is provided by the Advanced Composition Explorer (ACE), Global Geospace Science's Wind (WIND), Solar and Heliospheric Observatory (SOHO), and Deep Space Climate Observatory (DSCOVR). Over the last few decades, several models have been proposed to predict the occurrence of high-energy SEP events during satellite operations based on various observed datasets.

SPENVIS is particularly useful for providing solar particle fluences expected for the total mission duration and solar particle peak fluxes expected for individual events. SPENVIS operates the following models for solar protons fluences:

- the King model [19];
- the Jet Propulsion Laboratory (JPL-91) model [20];
- the Rosenqvist et al. (2005, 2007) model [21,22];
- the Emission of Solar Protons (ESP) total fluence and worst case event models [23,24];
- the Solar Accumulated and Peak Proton and Heavy Ion Radiation Environment (SAPPHIRE) total fluence and worst case models [25];

To be considered using SPENVIS, the entire prediction period for a mission should fall within the solar maximum phases of a solar cycle. The 7-year period of maximum solar activity is split as 2.5 years before and 4.5 years after the solar peak. Conservative estimate practice dictates use of fluences for one year for missions of shorter durations, if foreseen in the solar maximum phase. The confidence level represents the probability (in percentage) that the predicted proton fluences will not be exceeded. The confidence level ranges from 50% up to an upper limit, which depends on the selected model. When the planet has a magnetic field, the field shields solar particles. Simulation of the environment outside the magnetosphere of such planets is possible by disabling the software parameter for the shielding effect.

The **King solar proton** model was developed using data collected solely during the period 1966–1972, which were the active years of solar cycle 20. However, the Sun's activity during that cycle differed from that observed in cycle 19. Specifically, the largest annual mean sunspot number of cycle 19 was significantly greater than that of cycle 20. Moreover, the events during cycle 19 were much more frequent and intense than in the subsequent cycle. Assuming a linear relationship between sunspot number and annual integrated solar proton fluence, King decided to exclusively use the measurements acquired in cycle 20 as representative of cycle 21, while disregarding the data set of solar cycle 19.

The data set considered by the King model was mainly collected from measurements for the proton with energies in the range 10–100 MeV. The data were acquired by instruments on Interplanetary Monitoring Platform (IMP) 4, 5, and 6, which were all positioned in geocentric, highly elliptical orbits. In the King model, 25 individual events were used, including the outstanding event of August 1972, which accounted for nearly 70% of the total fluence of protons with energies over 10 MeV, as evaluated for the entire solar cycle. Since this great event contributed so significantly to the entire solar cycle fluence, King chose to distinguish it from the remaining 24 events and classified it as an anomalously large (AL) event.

The King model calculates the mean fluence for AL events, ordinary events (OR), and a worst-case spectrum. The last corresponds to the maximum intensity expected in the interplanetary environment near Earth (with a 90% confidence level) as the result of an OR. When the King model is used in SPENVIS, the number of AL and OR events can be

specified directly, rather than being derived from Burrell statistics. SPENVIS also calculates the confidence level result for the probability that the indicated number of events will not be exceeded. Using Burrell's extension of Poisson statistics, the number of events occurring during the mission can be calculated, determining the minimum number of events required to be counted in. The total event fluence is therefore the product of the number of predicted events and the AL or OR spectra.

It is worth noting some questionable assumptions of the King model. Primarily, the omission of data from solar cycle 19 was not justified, because of the casual character of cycles in general, which was confirmed in particular by the history of cycle 21. Furthermore, the net split-up of solar events into AL and OR classes appears somewhat artificial, especially when considering the major events of cycles 19 and 21. Additionally, the fact that during cycle 20 the number of recorded events was relatively low supports the limited statistical validity of the model. To address these drawbacks, Feynman and colleagues developed the JPL model [26]. Firstly, the differentiation between anomalously large (AL) and ordinary events was abolished, and the dataset was extended. For the first version of the JPL model (**JPL-85**), Feynman et al. used observations made by several spacecraft from 1963 to 1985. This period is three times longer than that used in the King model and includes three solar cycles. Later, the JPL-85 was replaced by its newer version, **JPL-91** [20] which comprises fluxes of protons with energies exceeding thresholds of 1, 4, 10, 30, and 60 MeV recorded nearly continuously; the daily average for those days during which the corresponding total fluence threshold was exceeded. Defined as the total fluence, the thresholds are 10, 5, 1, 1, and 1  $\text{cm}^{-2} \text{s}^{-1} \text{sr}^{-1}$  for the aforementioned five energy thresholds. For both JPL models, quiet periods were assumed to have no significant proton fluences; therefore, the data were collected exclusively over the seven active years of cycles. Based on the measurements of solar proton fluences acquired at the IMP-8, GOES-7, and GOES-8 spacecraft for all events from January 1974 to May 2002, the fluence values were updated in the energy ranges  $>10$  MeV [21] and  $>30$  MeV [22].

These updated values are used by the model **Rosenqvist et al.** [21] implemented in SPENVIS, which combines them with the JPL-91 parameter values for three other energy ranges ( $>1$  MeV,  $>4$  MeV and  $>60$  MeV). Depending on the mission duration, Kazama and Goka [27] recommend using higher confidence levels for shorter missions and 50–75% for durations longer than 7 years when using JPL.

The King, Rosenqvist and JPL models are valuable tools for predicting event fluences degradation over long-term missions. However, they unavoidably suffer from limitations due to incompleteness of the data sets laying in their bases. The limitation in the proton energy range is one of the most important. Fluence levels below 10 MeV are crucial to know for accurately predicting degradation of thin film photonic devices and solar cells. On the other hand, higher energy protons, capable of penetrating shielding, are important for assessing total dose degradation and single event effects in onboard electronics. Another limitation is that none of these models include data from all three solar cycles, 20, 21, and 22, despite high-quality space data being available for these cycles. This is significant because each cycle differed from the others. While cycle 22 was highly active with several very large events, cycle 20 had only one yet anomalously large event, and cycle 21 had no such large events at all.

The **ESP (Event Solar Proton)** model addresses these limitations by incorporating solar proton event data from all three complete recent solar cycles, from cycle 20 through cycle 22. For cycle 20, data were sourced from the IMP-3, -4, -5, -7, and -8 satellites. IMP-8 provided data for cycle 21, while data from the GOES-5, -6, and -7 satellites, which cover higher proton energies, were used for cycle 22. Only events with a certain minimum fluence value were considered. These last values were defined differently for different proton energy ranges [18] and are listed in Table 1 at the link <https://www.spervis.oma.be/help/background/flare/flare.html#ESP> (accessed on 15 May 2024).



**Table 1.** Simulation models available in SPENVIS for the solar proton fluences and peak fluxes.

Simulation	Model	Data Set	Measurements	Model Energy Range (MeV)
Solar protons fluences	King	Solar cycle 20	IMP 4, 5, 6 10–100 MeV	0.10–500
	JPL-85	Solar cycles 19–21	Detectors flown on rockets and balloons	0.10–500
	JPL-91	From 1963 up to 1985	Several spacecrafts 1–100 MeV	0.10–500
	Rosenqvist	January 1974 to May 2002	IMP-8, GOES-7 and GOES-8 1–100 MeV	0.10–500
	ESP	Solar cycles 20–22	IMP-3, -4, -5, -7, -8 GOES-5, -6, -7	0.10–500
	SAPPHIRE	1973–2013	SEPEM Reference Data Set (RDS) from GOES and SMS 0.1 MeV/nuc up to 1 GeV/nuc	0.10–500
Solar particle peak fluxes	CREME 86	<ul style="list-style-type: none"> <li>• Peak ordinary flare flux and mean composition</li> <li>• Peak ordinary flare flux and worst-case composition</li> <li>• Peak 10% worst-case flare flux and mean composition</li> <li>• Peak 10% worst-case flare flux and worst-case composition</li> <li>• Peak 4 August 1972, flare flux and mean composition</li> <li>• Peak 4 August 1972, flare flux and worst-case composition</li> <li>• Peak composite worst-case flare flux and mean composition</li> <li>• Peak composite worst-case flare flux and worst-case composition</li> </ul>		0.10–500
	CREME 96	<ul style="list-style-type: none"> <li>• 19–27 October 1989 episode</li> <li>• Worst week: flux averaged over 180 h beginning at 1300 UT on 19 October 1989</li> <li>• Worst day: flux averaged over 18 h beginning at 1300 UT on 20 October 1989</li> <li>• Worst 5 min: peak flux averaged over 5 min observed in October 1989</li> </ul>	GOES for protons IMP for heavy ions	
	Xapsos	Events 19, 22 and 24 October 1989		
	SAPPHIRE		SEPEM Reference Data Set (RDS)	

The Solar Accumulated and Peak Proton and Heavy Ion Radiation Environment (**SAPPHIRE**) model [20] built using the Solar Energetic Particle Environment Modelling (SEPEM) application server of ESA [28] provides the mission cumulative fluence, the largest Solar Particle Event (SPE) fluence and the SPE peak flux. The SAPPHIRE model exploits the SEPEM Reference Data Set (RDS v2.1), utilizing measurements from the energetic particle sensor (EPS) aboard the GOES series and analogous instruments aboard the earlier Synchronous Meteorological Satellite (SMS) series of NASA.

Concerning the solar particle peak fluxes simulation, the following models are available in SPENVIS:

- the CREME86 models [29];
- the CREME96 models [30];
- the Xapsos et al. (2000) model [24];
- the SAPPHIRE model [25].

For each model available in SPENVIS, simulation capabilities, data sets and spacecraft measurements employed are summarized in Table 1.

### 3. Relevant Standards: Documents Applied by ESA and CSA

#### 3.1. Relevant European Standards

The European Cooperation for Space Standardization (ECSS) is a teamwork between the European Space Agency, national space agencies and European industry associations, aiming to develop common standards for use by European actors for space business and research. In this context, two documents issued by the ECSS are particularly relevant, both of which are part of the System Engineering branch (ECSS-E-10) of the Engineering area of the ECSS system.

The “ECSS-E-ST-10-04C” standard [31] is envisioned to assist consistent specification of required and recommended methods of space environment engineering. It is aimed at ensuring best performance, problem avoidance or survivability of a product in the space environment. Its relevance in an international context relies in the capability (with its aggregated data, definitions and recommendations) of allowing existing organizational structures and methods to be applied in their specific context of effectiveness, and for the structures and methods to evolve as necessary without the need to re-define the standards. In particular, Section 9 (“Energetic particle radiation”) and Annex B (“Energetic particle radiation”) are referenced in the context of this work. In particular, the tables reported in the above-mentioned Annex represent a primary normative database at the international level for the definition of the energy distribution of space radiation.

The “ECSS-E-ST-10-12C” standard [32] covers methods for the calculation of radiation received and its effects, as well as a policy for design margins. In particular, Sections 3 (“Terms, definitions and abbreviated terms”), 4 (“Principles”), 7 (“Total ionizing dose”), and 8 (“Displacement damage”) are referenced in the context of this report. Its relevance in an international context relies on its focus in representing a viable standard to be applied for the management, engineering, and product assurance in space projects and applications.

#### 3.2. Relevant Chinese Standards

In the complexity of Chinese Standard systems, the formulation of conditions for space environmental tests requires application of multiple sources. First of all, the Chinese national standards GB (Guo Biao) [33] issued by the Standardization Administration of China (SAC), the Chinese National Committee of the International Organization for Standardization (ISO) and International Electrotechnical Commission (IEC), are mandatory to observe for any type of industrial or commercial activity. In specific cases of technical requirements for which no relevant national standards are available, the industrial standards (QB/T, FZ/T. . .) may be applied. Furthermore, the Corporation standards developed by Chinese corporations specifically operating in the field, such as the Chinese Aerospace Science and Technology Co. or Chinese Academy of Space Technology, provide supplementary rules for more detailed investigations and tests.

While the ISO standards arrange for the main rules for most space system tests like the acoustic, vibration, magnetic, thermal vacuum and thermal check on materials, the GB national standards are focused on the definition of the space environments and the environmental testing standards for spacecraft materials, for example GB Spacecraft environmental terminology or GB Solar electromagnetic radiation.

Among the Chinese standards for industrial use [34] issued by the Chinese state administration of science, technology, and industry for National Defense, the QJ branch collects standards [35] for aerospace applications. Similarly to ESA, ECSS and NASA relevant standards, dedicated QJ standards have been developed for space environmental testing

of spacecrafts, units, components and materials. They include more specified indications for the space environmental tests, in particular for the electron, proton, and ultraviolet radiations, the atomic oxygen and space debris impact, the outgassing and temperature effects. Both the single event effects and the total ionizing dosage are considered by these standards, and the monitored parameters of the environmental effects include the structural displacement damage, the atomic oxygen erosion, the contamination impact, etc.

For testing of thin film materials and multilayer coatings, we have determined the following QJ standards to be relevant. Their relevance in the international contest relies on their focus on specification of purposes and principles, general requirements, test conditions, samples, test procedures, test interruption or abnormality handling, data handling and test documents, with respect to the following radiation sources:

- QJ 20627-2016; Electron irradiation test method for space materials.
- QJ 20943-2018; Proton irradiation test method for space materials.
- QJ 20628-2016; Test method of combined radiation effects for space materials. It refers to combined irradiation test using electrons, protons and ultraviolet radiation.
- QJ 20424.3-2016; Environment test methods for spacecraft unit; Part 3: Solar ultraviolet irradiation test.

### 3.3. Key Concepts Operated in Existing Standards as Applied to Optical Coatings

Within these reference documents, the following key concepts have been defined:

Ionization is defined as the alternative interaction mechanism involving the excitation of its electrons rather than atom displacements. In common semiconductors and other solid-state/crystalline targets, it typically does not result in substantial structural effects. Common synonym: electronic interaction.

Displacement Damage (DD) is defined as the interaction occurring in materials and components due to the collision of the incoming radiation (or of secondary radiation generated within the target) with atoms of the target itself. When these collisions result in displacement events, structural defects such as vacancies and interstitials are generated. Such structural defects are characterized by different mobility depending on their type, the target material, and environmental parameters such as temperature. Therefore, they can remain as isolated defects, or alternatively cluster and/or react with impurities, thus creating relatively stable defects. DD has a direct effect on the degradation of mechanical (hardness, internal stresses, etc.), electronic (carriers lifetimes and mobilities), and optical (optical absorption, refractive index, etc.) properties of the target material, and therefore on its performance in relevant systems and devices. Common synonyms: non-ionizing damage, nuclear damage, nuclear interaction.

Energy Loss (EL) is defined as the amount of energy deposited in a material as a consequence of its exposure to a given radiation field. It is expressed in J (or more typically in eV) units. It can be further categorized as follows: (i) Ionizing Energy Loss (IEL): EL associated to ionization; (ii) Non-Ionizing Energy Loss (NIEL): EL associated to DD.

Dose is defined as the amount of energy deposited in a material per unit mass. It is typically expressed in Gy (i.e.,  $\text{J kg}^{-1}$ ), or alternatively in  $\text{MeV g}^{-1}$ . On the basis of the above-reported categorization between IEL and NIEL, it can be further categorized as follows: (i) Total Ionizing Dose (TID): dose associated to IEL; common synonym: ionizing dose; (ii) NIEL dose: dose associated to NIEL; common synonyms: Non-Ionizing Dose (NID), Total Non-Ionizing Dose (TNID).

Dose rate is defined as dose per unit of time.

Linear energy transfer (LET) is defined as the linear rate of energy deposited from a slowing energetic particle as a function of penetration depth in the target material. It is typically expressed in  $\text{eV } \text{Å}^{-1}$ , or through alternative energy (keV, MeV) and distance (nm,  $\mu\text{m}$ ) units.

Fluence (F) is defined as the key parameter quantifying the number of particles irradiating the target per unit surface over a given time interval. It is strictly related to the concept of Flux ( $\Phi$ ), which corresponds to the fluence per unit of time. In the case of



a multi-energetic radiation field, the energy dependence of the flux can be expressed in a differential form (i.e.,  $d\Phi/dE$ ).

Displacement Damage Equivalent Particle Fluence (DDEF) is defined as the fluence of a reference monoenergetic radiation field (namely, radiation type and energy), used to parameterize DD damage associated to different radiation fields, in the material under consideration. Typical radiation types adopted as a reference are protons, electrons or neutrons. Typical radiation energies are in the MeV range (e.g.: 1 MeV, 10 MeV, etc.) for bulk materials and in the tens of keV range for thin films.

By following the specific recommendations issued by the ECSS standardization body [32], the concept of Displacement Damage Equivalent particle Fluence (DDEF) allows for the parameterization of articulated radiation fields, including different ion species and energies.

For optical coatings, theoretical estimation of the particle radiation impact should be formulated using the aforementioned terms as a depth profile of the coating damage along the coating structure. To adequately reflect the specifics of optical thin films and multilayers, the layers should be graded in prediction of the foreseen induced optical degradation. The degradation profile varies with the energy of the impacting particles, upper layers being more affected by lower-energy particles, with deeper lying layers being more affected by higher energy particles. The impact on the substrate should be estimated too [36].

While real space environmental conditions where a coating is planned to be exploited are characterized by a typical continuous energetic spectra of particles in a certain range, on-ground tests employ quasi-monochromatic particle beams. Therefore, to render on-ground tests representative for a certain coating design, a fine theoretical estimation of the in-depth particle impact should be first performed when knowing the materials the coating consists of and the coating multilayer design. Notice, however, that thanks to introduction of the DDEF concept, the coatings can be tested by one particle type only.

#### 4. Consequent Guidelines for Radiation Tests

This section describes the guidelines for the radiation tests on the optical coatings we elaborated upon, and the comparison and analysis of the relevant European and Chinese standards. The results of this analysis have provided us with the general approach for suitable and representative tests specifically focused on the space environment impact on thin film's optical and optoelectronic devices. Furthermore, we discuss how the applied approach leads to an improvement in the existing standard procedure of the environmental tests for this specific type of spaceborne component, aiming for its optimization and increase in reliability.

The proposed protocol allows the quantitative prediction of the variation of the optical absorption properties of testbed materials resulting from irradiation with complex multi-energy and multi-species ion radiation fields, with a specific relevance to applications in aerospace.

The parameterization of induced structural damage is based on the concept of volumetric density of induced vacancies, as predicted by the SRIM Monte Carlo simulation code. The parameterization is based on a first-order approximation in which the optical absorption variation is assumed to be proportional to the density of induced defects and therefore to the irradiation fluence. As widely demonstrated, this approximation is largely valid for realistic irradiation conditions in the aerospace environment.

The model is based on a set of calibration data that needed to be acquired experimentally by systematically measuring the variation in optical absorbance in the material under analysis with a specific radiation field, that should preferably be mono-energetic and mono-species, at variable fluence. To this scope, the present work referred to specific papers from the scientific literature, i.e., [37] for  $Al_2O_3$ . The reported protocol can be effectively translated to the modelling of other macroscopic physical properties in the fields of optics (refractive index) and mechanics (Young's modulus, stiffness, etc.), as well as to model thermal properties (conductivity, etc.).

Structural damage in transparent materials results in the introduction of defect-associated electronic states in their forbidden gap, which in turn are responsible for the activation of optical absorption mechanisms. The progressive increase in the optical absorption coefficient and the variation of the absorption spectrum (coloration) constitutes predominant optical effects of DD from space radiation, as explicitly highlighted in Table 7-1 (“Technologies susceptible to total ionizing dose effects”) of [32].

Systematic studies of these phenomena have been carried in various classes of technologically relevant materials by adopting different types of damaging radiation (electrons, ions, neutrons) under substantially different irradiation conditions. In this context, the possibility of adopting a DD parameterization strategy compliant to ECSS standards (see Sections 3 and 5) offers the possibility of directly referring to such studies in the effort to model the variation of the optical properties of technologically relevant materials subjected to realistic space radiation fields.

In general, the irradiation-induced variation of optical properties in this material is probably associated with intrinsic or extrinsic defects, which are assigned to defective complexes such as the so-called F-type defects (i.e., electrons trapped with anion vacancy). However, the dynamic behavior of radiation-induced defects under implantation has not been fully clarified [38].

Optical absorbance is assumed to be proportional to the density of irradiation-induced defects. Furthermore, the surface density of irradiation-induced defects is assumed to be directly proportional to the irradiation fluence, at least for relatively low damage levels, such as the ones explored in this study. Under these approximations, the depth profile of the density of induced vacancies can be estimated by taking into due consideration the irradiation fluence  $F$ , i.e., the number of primary particles of the radiation field ( $\#_p$ ) per unit surface area ( $S$ ) of the target material:

$$\rho_v(z) = F \cdot \lambda(z) = \frac{\#_p}{S} \cdot \left( \frac{d\#_v}{dz} \right)_{nucl} \cdot (\#_p)^{-1} = \frac{1}{S} \cdot \left( \frac{d\#_v}{dz} \right)_{nucl}, \quad (1)$$

where  $\lambda(z)$  is the linear density of induced vacancies per ion and  $\#_v$  is the number of induced vacancies, which can be modeled with SRIM code.

Under this approximation, the cumulative DD is unaffected by complex non-linear effects, such as vacancy-interstitial recombination, damage saturation, and defect-defect interaction. Such effects would instead lead to sub-linear saturation effects at high damage densities. This assumption is therefore acceptable at relatively low irradiation fluences, and as such it is endorsed by the recommendation expressed in Section 8.5.2.2 (letter “a.1”) of [32].

The total number of induced vacancies per incoming ion can be expressed by the following integral:

$$n_v = \int_0^{z_{max}} \lambda(z) dz \quad (2)$$

On the basis of the above-mentioned linearity assumptions, the optical absorbance variation of the irradiated sample can be expressed as follows:

$$\Delta A = \int_0^d \Delta \alpha(z) dz = \int_0^d [k \cdot \rho_v(z)] dz \quad (3)$$

where  $d$  is the sample thickness and  $k$  is defined as the incremental absorption coefficient in the damaged regions of the material per unit of volumetric density of induced vacancies.

By combining Equations (1)–(3), it is possible to obtain the incremental absorbance per unit irradiation fluence  $K$ :

$$K = k \cdot n_v \quad (4)$$

It is worth remarking that, while the  $K$  parameter is inevitably specific to the above-mentioned target material and radiation field under consideration, the  $k$  parameter is only specific to the target material, while it has a general valence with regards to the

radiation field, since it results from a parameterization process which is not dependent on the ion species and energy. This enables the implementation of the DDEF concept. In this framework, if a complex radiation field is to be taken in consideration, the following procedural steps can be followed: (i) the radiation field is subdivided on the basis of the different ion species under consideration by taking into specific consideration the interplay between the higher structural damaging power and lower cosmic fluxes of heavier ions with respect to lighter ones; (ii) for each ion species, the (typically energy-differential) energy spectrum of ion fluxes values is subdivided into suitable energy bins, and (by considering a specific time exposure) a specific fluence value is determined for each energy bin; (iii) for each fluence value, the corresponding DDEF can be determined according to the above-described procedure; (iv) by using a suitable conversion factor from damage density to the differential variation of the optical parameter of interest (e.g., the optical absorption coefficient: see for example the case study reported in Section 5), the total absorbance variation is estimated for the radiation field under consideration, for a specific exposure time.

It is worth remarking that, despite the above-mentioned equivalence, the depth profile of the linear vacancy density induced by 10 MeV protons is different from the profiles referred to 60 keV He<sup>+</sup> ions and to 66 keV protons, see Section 5. The same applies to the overall profile (penetration depth, end-of-range peak height and width, etc.) of the optical absorption coefficient variation resulting from a 10 MeV proton irradiation carried at the DDEF fluence value. Nonetheless, it is worth remarking that the depth integral of such a profile (i.e., the overall absorbance variation of the irradiated sample) is equal to the one resulting from the integration of the corresponding profile for the reference radiation field. In other terms, and specifically for the case of the modeling of space radiation in thin films, it is important to remark that the DDEF concept must be applied by considering only the conversion of the fraction of energy loss occurring over the limited layer thickness. This is particularly relevant when high-energy and/or low-atomic-number ions are considered, whose penetration power is significantly increased with respect to low-energy and/or high-atomic-number ions, which in turn are mostly affecting the films. It is therefore important to take into account the layer thickness in order to avoid a DDEF-parameterized conversion of the energy loss occurring in the substrate.

A further remark is necessary about the role of ionizing energy loss; i.e., the fraction of ion energy loss resulting in electronic excitation/ionization rather than in nuclear collisions. Such energy loss is assumed to result in negligible structural effects, since its primary relaxation mechanism involves energy transfer to vibrational modes in the target crystals (i.e., ultimately a temperature increase). For the relatively low ion fluxes under consideration in space applications, target thermalization is assumed to occur at temperatures which are low enough to allow ruling out thermal effects. This assumption can potentially have exceptions if we consider the effects of the so-called swift-heavy-ions (SHI); i.e., ions characterized by a very high atomic number and extremely large energies (i.e., >100 MeV). In these cases, the interaction of even a single SHI with the target material can result in a structural effect, due to interaction mechanisms known as “thermal spiking” and “coulomb explosion”. In the former one, the temperature transient is so fast and localized that effective heat dissipation is not possible and localized (i.e., across the single ion track) melting of the target material is possible. In the latter, the instantaneous electrostatic repulsion of a high-density “cloud” of excited electrons along the ion track determines a structural shock that can result in localized damage. The modeling of SHI effects in target samples goes beyond the scope of the present work, particularly in consideration of their extremely low fluxes in space environments.

Energy- and solid-angle-differential fluxes of solar protons in interplanetary environments in “worst week” condition, resulting from the CREME-96 database reported in Table B-12 of [31], covers the range 1–1000 MeV. For lower energies, less information is available. Indeed, irradiation with protons in the 10–100 keV range can be relevant in this context, not only due to the contribution of this radiation field to the whole solar ion spectrum, but

specifically because of the possibility of delivering this type of irradiation in a laboratory context with the purpose of testing the radiation-induced modification of optical properties of materials and devices in a controlled environment. To this scope, in the present report we will specifically focus on the differential fluxes reported in [17].

We report in Table 2 the energy-binned fluence values for a 10-year exposure time of solar protons for the “Geotail 90%” dataset, for the two data points corresponding to <100 keV energy.

**Table 2.** Energy-dependent average solar proton fluences (“worst week” conditions) resulting from the differential fluxes with a time exposure of 10 years. The same number of induced vacancies per single incoming particle is reported in the third column.

Energy-Dependent Average Proton Fluences		
Energy Bin [keV]	Average Fluence [ $10^{11} \text{ cm}^{-2}$ ]	$n_v$
50–75	6.204	12
75–100	3.774	

## 5. Damage-Induced Variation of the Optical Properties of Al<sub>2</sub>O<sub>3</sub> Coatings on Crystalline Silicon and on Fused Silica Substrates

This section provides a representative example of rigorous application of the developed methodology described in previous sections. Single layers of amorphous aluminum oxide on fused silica substrates and on crystalline silicon substrates have been investigated for the impact of interplanetary particle radiation. Lagrange point L1 was considered as a possible mission environment, suggesting the use of  $10^{15} \text{ p/cm}^2$  fluence for the 40 keV protons available for the experimental setup. Energy- and solid-angle-differential fluxes of solar protons at the 50% and 90% cumulative probabilities obtained from the cumulative distribution curves obtained from the EPAM/LEMS120 (on board ACE) and EPIC-ICS (on board Geotail) spacecrafts over a common acquisition time period are reported in ref. [17]. The two flux values adopted for interpolation in this study were the ones represented by asterisk-shaped points at the extreme left of the plot of the Geotail 90% line in Figure 9 from [17].

As a first case study, Al<sub>2</sub>O<sub>3</sub> will be taken under consideration, because this material represents a useful testbed material, due to both its technological relevance in optical components for space applications and its high chemical and thermal stability [39]. Previous studies have achieved substantial progress in understanding many aspects of the effect of ion irradiation in Al<sub>2</sub>O<sub>3</sub>. Luminescence studies indicated that intrinsic optically-active defects can be activated by excited electrons [40]. In [41], the optical and thermal properties of anion vacancies in  $\alpha$ -Al<sub>2</sub>O<sub>3</sub> were extensively summarized, as well as electrical conduction. It has been conclusively demonstrated that the luminescence evolution in this material with the ion fluence exhibits two different behaviors due to two concomitant mechanisms, namely a conversion between F and F<sup>+</sup> defects and a destruction of both luminescent species resulting from the radiation-induced damage [42]. Also, in situ analysis of ion-induced luminescence in terms of incident ion energy and fluence was employed to effectively investigate the mechanism and/or origin of the luminescence [43], while transmission electron microscopy was used to study the microstructure features, defect diffusion, and cluster formation at a series of annealing temperatures.

In [37], the evolution of the optical absorption properties of Al<sub>2</sub>O<sub>3</sub> samples exposed to 60 keV He<sup>+</sup> ion irradiation has been investigated. More specifically,  $\alpha$ -Al<sub>2</sub>O<sub>3</sub> single crystals of (0001) orientation of  $10 \times 10 \times 0.5 \text{ mm}^3$  with optically polished surfaces were implanted at room temperature at fluences in the  $(5\text{--}100) \times 10^{16} \text{ cm}^{-2}$  range using a conventional ion implanter. Ion current density was  $17 \mu\text{A cm}^{-2}$ , and optical absorption spectra were acquired at room temperature with a Perkin-Elmer Lambda 950 UV/Vis/NIR spectrophotometer, as reported in Figure 4 of [37].

Figure 1 reports the fluence-dependent variation in optical absorbance at a 600 nm wavelength with respect to the value measured in the unirradiated sample, as extracted

from the data reported in Figure 4 of [37]. A linear dependence is clearly observable for the three datapoints lying at the lowest fluence values. The linear fitting procedure (red line in Figure 1) yields the following result:

$$\Delta A = K \cdot F = (1.550 \pm 0.006) \times 10^{-18} \cdot F[\text{cm}^{-2}]. \quad (5)$$

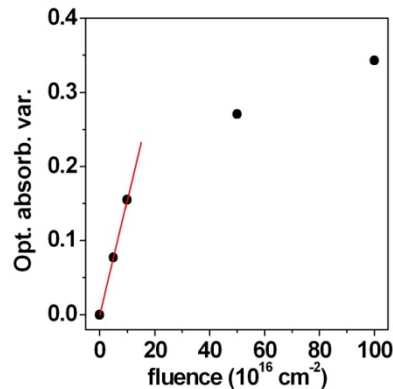


**Figure 1.** Optical absorbance increase (with respect to the non-irradiated sample) of  $\text{Al}_2\text{O}_3$  at a 600 nm wavelength as a function of 60 keV  $\text{He}^+$  irradiation fluence. Black dots report the experimental data as extracted from the data reported in Figure 4 of [37], while the red line reports the linear fitting function relevant to the three datapoints at the lowest fluence values.

The observed linear dependence for low damage levels is entirely compatible with the linearity assumption described in Section 4.

The depth-dependent linear density of induced vacancies for a single 60 keV  $\text{He}^+$  ion is reported in Figure 2.

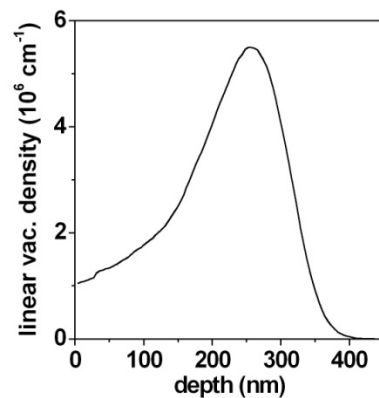


**Figure 2.** Linear density of induced vacancies in  $\text{Al}_2\text{O}_3$  from 60 keV  $\text{He}^+$  ion implantation, as obtained from the SRIM simulation. Note that the simulation is descriptive of the average effect of one incident particle.

From the  $K = (1.550 \pm 0.006) \times 10^{-18} \text{ cm}^2$  value reported in Equation (5), and from the  $n_v = 103$  value that can be obtained with SRIM, it is possible to estimate the  $k = (1.505 \pm 0.006) \times 10^{-20} \text{ cm}^2$  value from Equation (4).

On the basis of the value of the  $k$  parameter, it is possible to estimate the depth profile of the variation in the optical absorption coefficient of the target material. In this framework, it is possible to predict the variation in optical absorption caused by a different radiation field (i.e., 66 keV protons) at any given fluence  $F$  (for sake of example,  $F = 1 \times 10^{14} \text{ cm}^{-2}$ ).

For the different radiation field under consideration, the specific  $K$  value is given by Equation (4), in which  $n_v$  is now the total number of induced vacancies per incoming 66 keV proton, namely  $n_v = 12$  vacancies/ion.



From Equation (4), we thus obtain  $K = (1.81 \pm 0.07) \times 10^{-18} \text{ cm}^2$  for 66 keV protons. Now if a  $F = 1 \times 10^{14} \text{ cm}^{-2}$  fluence of 66 keV protons is considered, it is possible to plot the corresponding depth-dependent variation in the optical absorption coefficient for 600 nm wavelength of the incident light, as reported in Figure 3.

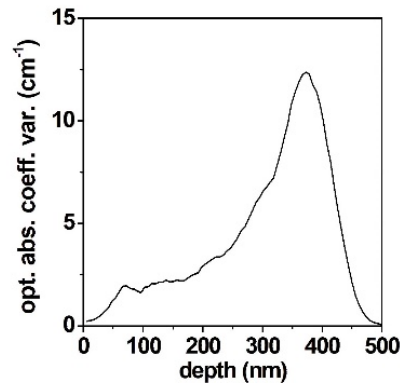


**Figure 3.** Depth profile of optical absorption coefficient variation ( $\Delta\alpha$ ) induced by a 66 keV proton implantation carried at a  $F = 1 \times 10^{14} \text{ cm}^{-2}$  fluence.

These results provide a protocol for the parameterization of structural damage (and thus of the corresponding variation in optical absorption coefficient, on the basis of the results reported in [37]) in  $\text{Al}_2\text{O}_3$  upon irradiation with any mono-species and mono-energetic ion radiation field.

We have performed an experiment [36] where 190 nm-thick amorphous alumina layers grown by atomic layer deposition (ALD) technique were irradiated by 40 keV protons at  $10^{15} \text{ p/cm}^2$  fluence. The induced change in the optical properties of the layer material modeled in terms of variation of its extinction coefficient, is illustrated in Figure 4, for five chosen wavelengths of the incidence light, from 300 nm through 900 nm.

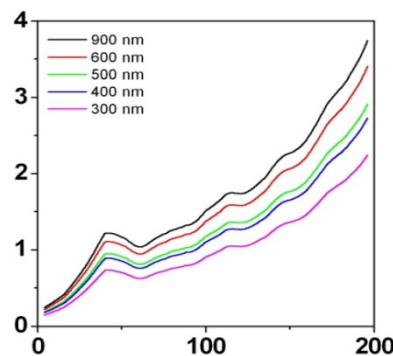


**Figure 4.** Depth profile of extinction coefficient variation ( $\Delta k$ ) modeled as induced by a 40 keV proton implantation of an amorphous alumina layer, carried at a  $F = 1 \times 10^{15} \text{ cm}^{-2}$  fluence.

The films were grown on two types of substrates, and the particles' impact on the film was different for the two substrate types. We will provide more details on this experimental study in a dedicated article. The interpretation of the impact of the irradiation on the coatings greatly depends on the correctness of the model, and the impact on the substrate material should be considered first [44]. We anticipate here that the predicted variations of the extinction coefficient of the order  $10^{-5}$ , see Figure 4, cannot be verified by using only commercial spectrophotometry, where typical sensitivity and accuracy are lower by two orders of magnitude.

## 6. Conclusions

Here, we proposed a methodology for estimation of the impact of energetic particles on the optical coatings, starting from the applicable standards adopted by the ESA and CSA.

We considered the deep space environment of Lagrange point L1 and provided relevant observations based on the space weather models implemented by major space agencies, and specifically by the ESA and CSA, when estimating the level of particle fluxes, energies and fluencies at L1.

Furthermore, we proposed here a protocol for representative on-ground testing of the optical coatings, including multilayer optical coatings, aiming in particular to estimate the particle radiation impact on the optical performance of the coatings in terms of the induced optical absorption.

The methodology we propose uses the DDEF concept, which enables the tests of the coatings by one particle type only. It imposes an a priori theoretical estimation of the particle radiation impact as a depth profile of the coating damage along the coating structure and inside the substrate. This degradation profile varies with the energy of the impacting particles, upper layers being more affected by lower-energy particles, with deeper-lying layers being more affected by higher energy particles. As the real space environment is characterized by typical continuous energetic spectra of particles in a certain range, to render on-ground quasi-monochromatic tests representatively, a fine theoretical estimation of the in-depth particle impact should be performed before the experiment, knowing the materials the coating consists of and the coating multilayer design.

**Author Contributions:** Conceptualization, A.S.; methodology, A.S.; formal analysis, A.S., M.L.P. and P.O.; investigation, A.S., M.L.P., P.O., Z.S. and Y.W.; resources, A.S. and Y.W.; data curation, A.S., M.L.P., P.O., Z.S. and Y.W.; writing—original draft preparation, A.S., M.L.P. and P.O.; writing—review and editing, A.S., M.L.P., P.O., Z.S. and Y.W.; visualization, P.O. and M.L.P.; supervision, A.S. All authors have read and agreed to the published version of the manuscript.

**Funding:** This work was supported by the Italian Ministry for University and Research and the Italian Ministry of Foreign Affairs: PGR project AstroOptElect and by the National Key R&D program of China: 2018YFE0118000.

**Data Availability Statement:** Data may be available at reasonable request.

**Conflicts of Interest:** The authors declare no conflict of interest.

## References

1. Freeman, A. Exploring our solar system with CubeSats and SmallSats: The dawn of a new era. *CEAS Space J.* **2020**, *12*, 491–502. [[CrossRef](#)]
2. Poghosyan, A.; Golkar, A. Cubesat evolution: Analyzing cubesat capabilities for conducting science missions. *Prog. Aerosp. Sci.* **2017**, *88*, 59–83. [[CrossRef](#)]
3. Gadisa, D.; Bang, H. Small Satellite Electro-Optical System (EOS) Technological and Commercial Expansion. *Acta Astronaut.* **2023**, *213*, 355–372. [[CrossRef](#)]
4. Available online: <https://www.nasa.gov/artemis-accords/> (accessed on 15 May 2024).
5. Available online: [https://www.unoosa.org/documents/pdf/copuos/2023/TPs/ILRS\\_presentation20230529\\_.pdf](https://www.unoosa.org/documents/pdf/copuos/2023/TPs/ILRS_presentation20230529_.pdf) (accessed on 15 May 2024).
6. The Pierre Auger Collaboration. Observation of a Large-Scale Anisotropy in the Arrival Directions of Cosmic Rays above  $8 \times 10^{18}$  eV. *Science* **2017**, *357*, 1266–1270. [[CrossRef](#)] [[PubMed](#)]
7. Oran, R.; Landi, E.; van der Holst, B.; Lepri, S.T.; Vasquez, A.M.; Nuevo, F.A.; Frazin, R.; Manchester, W.; Sokolov, I.; Gombosi, T.I. A Steady-state Picture of Solar Wind Acceleration and Charge State Composition Derived from a Global Wavedriven MHD Model. *Astrophys. J.* **2015**, *806*, 55. [[CrossRef](#)]
8. Dubyagin, S.; Ganushkina, Y.N.; Sergeev, V. Formation of 30 keV proton isotropic boundaries during geo-magnetic storms. *J. Geophys. Res. Space Phys.* **2018**, *123*, 3436–3459. [[CrossRef](#)]
9. Sznajder, M.; Seefeldt, P.; Spröwitz, T.; Renger, T.; Kang, J.H.; Bryant, R.; Wilkie, W. Solar Sail Propulsion Limitations Due to Hydrogen Blistering. *Adv. Space Res.* **2020**, *67*, 2655–2668. [[CrossRef](#)]
10. Wertz, J.R. Modeling the Space Environment. In *Spacecraft Attitude Determination and Control*; Wertz, J.R., Ed.; Astrophysics and Space Science Library; Springer: Dordrecht, The Netherlands, 1978; Volume 73. [[CrossRef](#)]
11. Available online: <https://www.nasa.gov/nase/software> (accessed on 15 May 2024).
12. Lundstedt, H.; Wintoft, P.; Wu, J.-G.; Gleisner, H.; Døvheden, V. Space Environment Modelling with the Use of Artificial Intelligence Methods. *Eur. Space Agency* **1996**, *392*, 269.

13. Klein, E.M.; Sznajder, M.; Seefeldt, P. Proton Spectra for the Interplanetary Space Derived from Different Environmental Models. *Front. Space* **2022**, *3*, 933340. [[CrossRef](#)]
14. Fetzer, A.; Anger, M.; Oleynik, P.; Praks, J. Total ionising dose multilayer shielding optimisation for nanosatellites on geostationary transfer orbit. *Adv. Space Res.* **2024**, *73*, 831–845. [[CrossRef](#)]
15. Lei, F.; Truscott, R.R.; Dyer, C.S.; Quaghebeur, B.; Heynderickx, D.; Nieminen, R.; Evans, H.; Daly, E. MULASSIS: A Geant4-based multilayered shielding simulation tool. *IEEE Trans. Nucl. Sci.* **2002**, *49*, 2788–2793. [[CrossRef](#)]
16. Lagrange, J.L. Essai sur le Problème des Trois Corps, Euvres complètes, 1772. Volume 6, pp. 229–331. Available online: <https://gallica.bnf.fr/ark:/12148/bpt6k229225j/f231> (accessed on 15 May 2024).
17. Laurenza, M.; Alberti, T.; Marcucci, M.F.; Consolini, G.; Jacquy, C.; Molendi, S.; Macculi, C.; Lotti, S. Estimation of the Particle Radiation Environment at the L1 Point and in Near-Earth Space. *Astrophys. J.* **2019**, *873*, 112. [[CrossRef](#)]
18. Kruglanski, M.; Messios, N.; De Donder, E.; Gamby, E.; Calders, S.; Hetey, L.; Evans, H. SPace ENVIRONMENT Information System: SPENVIS. Available online: <https://www.spervis.oma.be/> (accessed on 15 May 2024).
19. King, J.H. Solar Proton Fluences for 1977–1983 Space Missions. *J. Spacecr. Rocket.* **1974**, *11*, 401. [[CrossRef](#)]
20. Feynman, J.; Spitalo, G.; Wang, J.; Gabriel, S. Interplanetary Proton Fluence Model: JPL 1991. *J. Geophys. Res.* **1993**, *98*, 13281–13294. [[CrossRef](#)]
21. Rosenqvist, L.; Hilgers, A.; Evans, H.; Daly, E.A.; Hapgood, M.; Stamper, R.; Zwickl, R.; Bourdarie, S.; Boscher, D. Toolkit for Updating Interplanetary Proton-Cumulated Fluence Models. *J. Spacecr. Rocket.* **2005**, *42*, 6. [[CrossRef](#)]
22. Glover, A.; Hilgers, A.; Rosenqvist, L.; Bourdarie, S. Interplanetary proton cumulated fluence model update. *Adv. Space Res.* **2008**, *42*, 1564–1568. [[CrossRef](#)]
23. Xapsos, M.A.; Summers, G.P.; Barth, J.L.; Stassinopoulos, E.G.; Burke, E.A. Probability Model for Worst Case Solar Proton Event Fluences. *IEEE Trans. Nucl. Sci.* **1999**, *46*, 1481–1485. [[CrossRef](#)]
24. Xapsos, M.A.; Summers, G.P.; Barth, J.L.; Stassinopoulos, E.G.; Burke, E.A. Probability Model for Cumulative Solar Proton Event Fluences. *IEEE Trans. Nucl. Sci.* **2000**, *47*, 486–490. [[CrossRef](#)]
25. Jiggins, P.; Varotsou, A.; Truscott, P.; Heynderickx, D.; Lei, F.; Evans, H.; Daly, E. The solar accumulated and peak proton and heavy ion radiation environment (SAPPHIRE) model. *IEEE Trans. Nucl. Sci.* **2018**, *65*, 698–711. [[CrossRef](#)]
26. Feynman, J.; Armstrong, T.P.; Dao-Gibner, L.; Silverman, S. New Interplanetary Proton Fluence Model. *J. Space-Craft Rocket.* **1990**, *27*, 403. [[CrossRef](#)]
27. Kazama, Y.; Goka, G. A New Modeling Method of Solar Energetic Proton Events for ISO Specification. *Adv. Space Res.* **2008**, *42*, 1293–1299. [[CrossRef](#)]
28. Crosby, N.; Heynderickx, D.; Jiggins, P.; Aran, A.; Sanahuja, B.; Truscott, P.; Lei, F.; Jacobs, C.; Poedts, S.; Gabriel, S.; et al. SEP-EM: A tool for statistical modeling the solar energetic particle environment. *Space Weather* **2015**, *13*, 406–426. [[CrossRef](#)]
29. Adams, J.H.; Silberberg, R.; Tsao, C.H. Cosmic Ray Effects on Microelectronics. *IEEE Trans. Nucl. Sci.* **1982**, *29*, 169–172. [[CrossRef](#)]
30. Tylka, A.J.; Dietrich, W.F.; Boberg, P.R. Probability Distributions of High-Energy Solar-Heavy-Ion Fluxes from IMP-8: 1973–1996. *IEEE Trans. Nucl. Sci.* **1997**, *44*, 2140–2149. [[CrossRef](#)]
31. ECSS-E-ST-10-04C; Space Engineering–Space Environment. Secretariat of the European Cooperation of Space Standardization, ESA-ESTEC, Requirements and Standards Division: Noordwijk, The Netherlands, 15 June 2020.
32. ECSS-E-ST-10-12C; Space Engineering–Methods for the Calculation of Radiation Received and Its Effects, and a Policy for Design Margins. Secretariat of the European Cooperation of Space Standardization, ESA-ESTEC, Requirements and Standards Division: Noordwijk, The Netherlands, 15 November 2008.
33. Available online: <http://www.sac.gov.cn/sacen/Standards/> (accessed on 15 May 2024).
34. Available online: <https://www.standardsofchina.com/professional> (accessed on 15 May 2024).
35. Available online: [https://www.standardsofchina.com/standard\\_list/QJ](https://www.standardsofchina.com/standard_list/QJ) (accessed on 15 May 2024).
36. Sytchkova, A.; Olivero, P.; Protopapa, M.L.; Shen, Z.; Wang, Z.; Zhang, K.; Wang, Y.; Buresi, E.; Palmisano, M.; Pesce, E.; et al. Proton-induced damage in ALD-deposited Al<sub>2</sub>O<sub>3</sub> thin films for space applications: Dependence on substrate material. In Proceedings of the European Optical Society Annual Meeting EOSAM 2021, TOM 6 Optical Materials: Crystals, Thin Films, Organic Molecules and Polymers, Syntheses, Characterization and Devices, n. 489, Rome, Italy, 13–17 September 2021.
37. Zhong, M.; Yang, L.; Yang, G.; Yan, Z.; Li, Z.; Zheng, W.; Yuan, X.; Guo, D.; Huang, J.; Xiang, X. Dose-dependent optical properties and laser damage of helium-implanted sapphire. *Can. J. Phys.* **2014**, *93*, 776–783. [[CrossRef](#)]
38. Moritani, K.; Takagi, I.; Moriyama, H. Production behavior of irradiation defects in  $\alpha$ -alumina and sapphire under ion beam irradiation. *J. Nucl. Mat.* **2004**, *326*, 106–113. [[CrossRef](#)]
39. Xiang, X.; Zu, X.T.; Zhu, S.; Wei, Q.M.; Zhang, C.F.; Sun, K.; Wang, L.M. ZnO nanoparticles embedded in sapphire fabricated by ion implantation and annealing. *Nanotechnology* **2006**, *17*, 2636–2640. [[CrossRef](#)]
40. Al Ghamdi, A.; Townsend, P.D. Ion beam excited luminescence of sapphire. *Nucl. Instrum. Methods Phys. Res. B* **1990**, *46*, 133. [[CrossRef](#)]
41. Evans, B.D. A review of the optical properties of anion lattice vacancies, and electrical conduction in  $\alpha$ -Al<sub>2</sub>O<sub>3</sub>: Their relation to radiation-induced electrical degradation. *J. Nucl. Mater.* **1995**, *219*, 202. [[CrossRef](#)]
42. Jardin, C.; Canut, B.; Ramos, S.M.M. The luminescence of sapphire subjected to the irradiation of energetic hydrogen and helium ions. *J. Phys. D Appl. Phys.* **1996**, *29*, 2066. [[CrossRef](#)]

43. Tanabe, T.; Fujiwara, M.; Miyazaki, K. Energetic particle induced luminescence of Al<sub>2</sub>O<sub>3</sub>. *J. Nucl. Mat.* **1996**, 233–237, 1344–1348. [[CrossRef](#)]
44. Sytchkova, A.; Protopapa, M.L.; Olivero, P.; Tapfer, L.; Burrese, E.; Dunatov, T.; Siketic, Z.; Palmisano, M.; Pesce, E.; Wang, Y.; et al. Optical characterization of the impact of 100 keV protons on the optical properties of ZrO<sub>2</sub> films prepared by ALD on fused silica substrates. *Appl. Opt.* **2023**, 62, B182–B187. [[CrossRef](#)] [[PubMed](#)]

**Disclaimer/Publisher’s Note:** The statements, opinions and data contained in all publications are solely those of the individual author(s) and contributor(s) and not of MDPI and/or the editor(s). MDPI and/or the editor(s) disclaim responsibility for any injury to people or property resulting from any ideas, methods, instructions or products referred to in the content.